PHYSICAL REVIEW E **76**, 046306 (2007)

Multiple zonal jets and drifting: Thermal convection in a rapidly rotating spherical shell compared to a quasigeostrophic model

Jon Rotvig[*]
Institut für Geophysik, ETH Zürich, CH-8093 Zürich, Switzerland

(Received 23 November 2006; revised manuscript received 28 May 2007; published 5 October 2007)

We demonstrate that thermal convection in a rapidly rotating spherical shell may produce zonal flows outside the tangent cylinder that consist of multiple alternating jets drifting towards the interior. A quasigeostrophic model that in model space is located between the classical annulus and the spherical shell, has been constructed. In this generalized annulus model we allow for terms in the Ekman correction to the flow that are usually neglected. It is shown that these terms may create observable effects at low Ekman numbers. Some of the remaining differences between the two-dimensional (2D) and 3D model may be explained by the missing heat transport along the rotation axis of the 2D model. The 2D model makes it possible to show that the occurrence of jet drift requires a significant radial dependence of the β parameter. In addition, the relatively low numerical costs of the 2D model allow extensive parameter studies. For an increasing rotation rate and fixed moderate thermal driving, the 2D model predicts (i) an increased zonal flow strength, (ii) an increased number of jets related to Rhines length scale, and (iii) an inward drift of the center jets. For an increasing thermal driving and fixed rotation rate, the solutions of the 2D model develop stronger zonal flows with a reduced number of still faster drifting jets. The jet drift is ultimately converted into fluctuations of a couple of steady jets as the center region outside the tangent cylinder is being cleared of jets. These solutions, that display reduced Ekman layer effects, resemble solutions obtained with stress-free boundary conditions.

DOI: 10.1103/PhysRevE.76.046306 PACS number(s): 47.27.−i, 47.32.Ef, 91.25.Cw

I. INTRODUCTION

Models of alternating zonal jets driven by rotating thermal convection has been a longstanding problem [1]. This problem is astrophysically motivated by the fact that cooling planets in their interior often possess rapidly rotating liquid shells consisting of iron or hydrogen and helium. On planets with an exposed liquid shell, differential rotation may be observed directly as banded structures, e.g., on the surface of Jupiter and Saturn. Recent progress on this problem have been reported in Refs. [2,3]. As long as the thermal driving is not too strong the tangent cylinder (TC) separates the fluid dynamics. The TC is defined as the imaginary cylinder along the rotation axis that touches the inner boundary of the shell. In the models of Refs. [2,3] it was necessary to impose stress-free boundary conditions at both surfaces in order to obtain an overall strong zonal flow. In the case where the inner boundary of the liquid shell is nonslip only weak zonal flows form inside the TC [4]. These findings illustrate the fact that the mechanical boundary conditions is one of the key model parameters of the problem.

For a stress-free outer boundary, the number of jets outside the TC is mostly 2, but sometimes only 1. Considering the surfaces of enclosed liquid planetary cores the appropriate boundary conditions are nonslip. This also applies to laboratory experiments on thermal convection in rotating spherical shells [5–7]. The Ekman layer drag at these rigid boundaries slows down the zonal flow in the entire shell. However, the qualitative properties of the zonal flow may change significantly: outside the TC, due to the rigid outer boundary, multijets, i.e., more than 2, may develop [7–9]. In the present paper we demonstrate that yet another model parameter determines the qualitative properties of the zonal flow: when the radial dependence of the geostrophic height of the container outside the TC is sufficiently strong the multijet solutions become unstable and the jets begin to drift towards the interior. The radial dependence of the β parameter that applies to the spherical shell is sufficient to destabilize the multijet zonal flows.

In dynamo simulations where the magnetic field is being induced by thermal convection in enclosed rotating liquid shells, stress-free boundary conditions have been employed in an attempt to reduce the damping of torsional oscillations and to strengthen the toroidal component of the magnetic field as this is the expected case at high rotation rates, see Ref. [10], and references therein. The argument that the viscous boundary layers may be dispensed with in simulations at low to moderate rotation rates has some relevance. However, as shown in the present paper, nonslip boundary conditions significantly affect the low Ekman number regime. A new type of flow with different dynamo properties develops. It therefore seems important to keep the mechanical boundary conditions in mind when still stronger computers and the development of simplified numerical dynamo models allow dynamo investigations at yet higher rotation rates.

In this paper we present aspects of multiple zonal jets in three-dimensional (3D) models and develop closely related 2D models that allow us to anticipate the fluid dynamics at higher rotation rate and thermal driving. In 3D we consider the kinematic dynamo properties of this type of flow.

II. MODELS

In the Boussinesq approximation, the problem of thermal convection in a rotating spherical shell is given by

---

[*] rotvig@erdw.ethz.ch

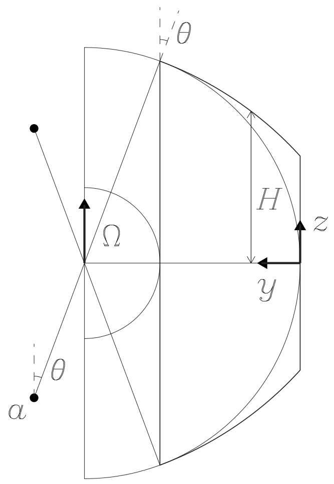

FIG. 1. Geometry of the 2D model. The top and bottom boundary of the duct are sections of cylindrical surfaces with radius r_T. In this plot $r_T = r_0/0.6$.

$$E\left(\frac{\partial \mathbf{u}}{\partial t} + \mathbf{u}\cdot\nabla\mathbf{u}\right) + 2\mathbf{e}_z \times \mathbf{u} = -\nabla P - \mathrm{Ra}\, g T \mathbf{e}_g + E\nabla^2\mathbf{u}, \tag{1a}$$

$$\frac{\partial T}{\partial t} + \mathbf{u}\cdot\nabla T = \frac{1}{\mathrm{Pr}}\nabla^2 T, \tag{1b}$$

where the flow $\mathbf{u}$ is incompressible, $\nabla\cdot\mathbf{u}=0$. The nondimensionalization is taken as in the spherical dynamo benchmark [11]. The Rayleigh, Ekman, and Prandtl numbers are $\mathrm{Ra} = \alpha g_0 \Delta T d/\nu\Omega$, $E=\nu/\Omega d^2$, and $\mathrm{Pr}=\nu/\kappa$, where (ν,κ) is the kinematic viscosity and thermal diffusivity. The thermal expansion coefficient is denoted by α. The shell thickness is d and the ratio between the inner and outer radius is $\xi = r_i/r_0 \equiv 0.35$, which has been set to the present value of the aspect ratio of the Earth fluid core. Thus the nondimensional $(r_i, r_0) = (\xi, 1)/(1-\xi)$. The container is rotating about the z axis with angular velocity Ω. We impose nonslip boundaries. The direction of gravity $\mathbf{e}_g = -\mathbf{e}_r$. The gravity profile $g = r/r_0$ has been normalized to one at the outer boundary. The system is heated at $r=r_i$ and ΔT denotes the temperature difference between the inner and outer boundary.The temperature $T=\tilde{T}+\hat{T}$ is decomposed into a thermally conductive basic state $\tilde{T}=r_i(r_0/r-1)$ and a perturbation $\hat{T}$, which is zero at the boundaries.

The 3D convection problem has been solved using a classical timestepping quasispectral code. This code is based on expansions in spherical harmonics and radial Chebyshev polynomials and has been developed from the Cartesian code used in Ref. [12]. The onset of convection problem was solved as a generalized eigenvalue problem [9].

In this paper we compare the spherical shell outside the TC to a quasigeostrophic model. The geometry of the 2D model may be described as follows. Two coaxial cylinders have their common axis parallel to the x axis, see Fig. 1. The distance between the cylinders is d and the ratio between their radii $\xi = r_i/r_0 \equiv 0.35$. A periodic duct of length L_x parallel to the x axis touches these cylinders at the equatorial plane. Thus we may expand the solution in the form $A = \sum_l A_l e^{ilx(2\pi/L_x)}$. A third cylinder with axis a parallel to the x axis defines the top boundary of the duct. It is tangential to the outer cylinder at the inner sidewall and has radius $r_T > r_0$. The top and bottom boundary are symmetric in the equatorial plane. Curvature about the rotation axis has been neglected allowing us to obtain the classical annulus in the limit where $r_T/r_0 \gg 1$ and $\xi \ll 1$. The value of Ra at onset of convection Ra_c is affected by the omission of azimuthal curvature. However, by taking $L_x = 2\pi r_i$, we obtain l wave numbers close to the azimuthal wave numbers in the 3D model at $\mathrm{Ra}=\mathrm{Ra}_c$. We may introduce a cylindrical coordinate system $\mathcal{C}_T$ in which the top boundary is a coordinate surface. The azimuthal axis of $\mathcal{C}_T$ is a and the polar axis is along the z axis. A point in this coordinate system is given by (r,θ,x). Note that the above r_T may refer to the system $\mathcal{C}_T$, whereas r_i and r_0 do not. The height of the top boundary above the equatorial plane is H and its angle of inclination is θ. These quantities satisfy $H = r_T(\cos\theta - \sqrt{1-\xi^2}) + \sqrt{(1+\xi)/(1-\xi)}$ and $\sin\theta = \xi + (1-y)/r_T$, hence $\partial_y H = \tan\theta$. To complete the geometry definitions we finally specify, in a way similar to the above, a cylindrical coordinate system $\mathcal{C}_B$ in which the bottom boundary is a coordinate surface.

In quasigeostrophic models the velocity and temperature are usually approximated by $\mathbf{u} = -\nabla\times V(x,y)\mathbf{e}_z + \mathbf{u}'(\mathbf{r})$ and $T=T(x,y)$, where $|\mathbf{u}'| \ll |\nabla\times V\mathbf{e}_z|$. Furthermore, we assume that $\mathbf{e}_g = \mathbf{e}_y$, $g=g(y)$, and $\tilde{T}=\tilde{T}(y)$. Let us consider a pair of points one of which is located at the top boundary while the second one is the reflection in the equatorial plane. No penetration at the top and bottom boundary implies that $u_z^{T,B} = \pm\tan\theta u_y^{T,B}$, respectively, where θ refers to the top point in system $\mathcal{C}_T$. By superimposing nonslip boundary conditions at these surfaces the mainstream $\mathbf{u}$ is being adjusted by viscous Ekman layers [13]. This bulk Ekman correction flow $\mathbf{v}$ is of order $O(E^{1/2})$. The component of $\mathbf{v}$ along the rotation axis at the top and bottom boundary is $v_z^{T,B} = \pm(v_r^{T,B}/\cos\theta + \tan\theta v_y^{T,B})$. Here $v_r^{T,B}$ refer to the radial component of $\mathbf{v}$ in $\mathcal{C}_T$ and $\mathcal{C}_B$, respectively. From Eqs. (1a), (1b) the z-averaged z vorticity equation and the heat equation then become

$$\frac{\partial\nabla^2 V}{\partial t} + J(V,\nabla^2 V) - \frac{2}{EH}\left[\tan\theta u_y + \frac{v_r}{\cos\theta} + \tan\theta v_y\right]_T = -\frac{\mathrm{Ra}}{E} g\frac{\partial\hat{T}}{\partial x} + \nabla^2\nabla^2 V, \tag{2a}$$

$$\frac{\partial\hat{T}}{\partial t} + J(V,\hat{T}) = -\frac{\partial V}{\partial x}\frac{\partial\tilde{T}}{\partial y} + \frac{1}{\mathrm{Pr}}\nabla^2\hat{T} + \frac{1}{\mathrm{Pr}}\nabla^2\tilde{T}. \tag{2b}$$

The Jacobian is defined by $J(A,B) = \partial_x A\partial_y B - \partial_y A\partial_x B$. For the Coriolis term at the boundaries, i.e., the third term in Eq. (2a), we used that u_y, v_r (in $\mathcal{C}_T$ and $\mathcal{C}_B$), and v_y are symmetric in the equatorial plane. For the symmetry of v_r and v_y see Eqs. (2.17.2), (2.6.16) in Ref. [13]. The Coriolis term in Eq. (2a) is evaluated at the top boundary.

To evaluate v_r at the top boundary we need $u_\theta = -(\cos\theta u_y + \sin\theta u_z)$. Here the last term may become important for $\theta \sim 1$. Neglecting or keeping this term, we find

$$\frac{v_r}{\cos\theta} = -\frac{E^{1/2}}{2}\left[\frac{1}{\cos^{1/2}\theta}\left(\frac{\partial u_y}{\partial x} - \frac{\partial u_x}{\partial y}\right) + \frac{1}{\cos^{3/2}\theta}\left(\frac{\partial u_x}{\partial x} + \cos^2\theta\frac{\partial u_y}{\partial y}\right) + \frac{\tan\theta}{2r_T\cos^{1/2}\theta}\left(\frac{u_x}{\cos\theta} + u_y\right)\right], \qquad (3a)$$

$$\frac{v_r}{\cos\theta} = -\frac{E^{1/2}}{2}\left[\frac{1}{\cos^{1/2}\theta}\left(\frac{1}{\cos^2\theta}\frac{\partial u_y}{\partial x} - \frac{\partial u_x}{\partial y}\right) + \frac{\tan\theta}{2r_T\cos^{1/2}\theta}\left(\frac{u_x}{\cos\theta} - \frac{3u_y}{\cos^2\theta}\right)\right], \qquad (3b)$$

respectively, see Eq. (2.17.2) in Ref. [13].

The third Coriolis subterm in Eq. (2a) may become comparable to minus the second subterm for $\theta \sim 1$. We derive an equation for v_y as follows. The first and third Coriolis subterm have the same form. Since the toroidal part of $\mathbf{u}$ is large we assume that the toroidal part of $\mathbf{v}$ may be neglected. This turns out to be a good approximation. From Eq. (2.6.16) in Ref. [13] we write $\partial_z \mathbf{v} \approx \nabla \times \nabla \times A(x,y)\mathbf{e}_z$. The poloidal potential of $\mathbf{v} = \nabla \times \nabla \times W\mathbf{e}_z$, then satisfies $\nabla^2 W = -1/2\{z(v_z^T - v_z^B)/H + v_z^T + v_z^B\}$. Hence

$$\nabla^2 v_y + \frac{\partial}{\partial y}\left[\frac{\tan\theta v_y}{H}\right]_T = -\frac{\partial}{\partial y}\left[\frac{v_r}{H\cos\theta}\right]_T. \qquad (4)$$

This equation is second order in y. We impose no-penetration boundary conditions at the sidewalls, $v_y = 0$ at $y = 0$ and $y = 1$.

Two sets of gravity and thermal basic state profiles have been investigated, profile A: $[g, \tilde{T}] = [1, y]$ and profile B: $[g, \tilde{T}] = [1 - (1-\xi)y, \xi y/\{1 - (1-\xi)y\}]$. Profile A corresponds to the classical annulus [8,9], and profile B to the spherical shell. The latter has been obtained from the spherical shell profiles by substituting $r = r_0[1 - (1-\xi)y]$. This, however, introduces a basic state diffusion term in Eq. (2b) which is not present in the 3D model. We cancel this term by a heat source.

The sidewalls, $y = 0$ and $y = 1$, are either both (i) stress-free walls or (ii) nonslip walls. In case (i) we impose $V = \partial_{yy}V = 0$. This implies that the y-averaged zonal flow is zero $\langle u_x\rangle_{xy} = -[\langle V\rangle_x(y=1) - \langle V\rangle_x(y=0)] = 0$, where $\langle A\rangle_b$ is defined as the b-average of the A quantity. We impose this additional condition in the stress-free case in order to obtain a model setup close to the annulus in Refs. [8,9]. This latter condition is relaxed in the case of nonslip sidewalls. In fact the y-averaged zonal flow may become large [14]. In case (ii) we impose $V = \partial_y V = 0$ for the nonzero azimuthal wave numbers. The boundary conditions for $l = 0$ are found from the zonal flow equation

$$\frac{\partial\langle u_x\rangle_x}{\partial t} + \frac{\partial\langle u_x u_y\rangle_x}{\partial y} = -\frac{E^{-1/2}}{H\cos^{1/2}\theta}\langle u_x\rangle_x + \frac{\partial^2\langle u_x\rangle_x}{\partial y^2} \qquad (5)$$

which is obtained by xz averaging the x component of the momentum equation (1a) and then expanding the Coriolis term in contributions from the duct endwalls $x = 0$ and $x = L_x$, the sidewall $y = 0$, and the top and bottom boundary. The latter contributions involve the Ekman suction at these boundaries. Note that the term $\left[\frac{E^{-1/2}}{H\cos^{1/2}\theta}\langle u_x\rangle_x\right]_{y=0}$ which also enters the right-hand side of Eq. (5) vanishes due to the nonslip sidewall. By y averaging Eq. (5) we find with $V(y=0) = 0$ that

$$\left.\frac{\partial V}{\partial t}\right|_{y=1} = -\left\langle\frac{E^{-1/2}}{H\cos^{1/2}\theta}\frac{\partial V}{\partial y}\right\rangle_y + \left.\frac{\partial^2 V}{\partial y^2}\right|_{y=1} - \left.\frac{\partial^2 V}{\partial y^2}\right|_{y=0} \qquad (6)$$

for $l = 0$. This condition together with $V(y=0) = 0$ and $\partial_y V = 0$ apply for $l = 0$. In the annulus model with nonslip sidewalls and free-slip, nearly plane-parallel top and bottom boundaries, a large $\langle u_x\rangle_{xy}$ may develop [14]. We have successfully tested our model using some of their cases. However, in the 2D models below, $\langle u_x\rangle_{xy}$ is negligible, as the kinetic energy ratio $\langle E_k(\langle u_x\rangle_{xy})/E_k(\langle u_x\rangle_x)\rangle_t < 1.2\%$.

The 2D models have been implemented by azimuthal plane wave expansions and radial second-order finite differences. Radial Chebyshev expansions were used to solve the problem at onset of convection, which, as in the 3D model above, constitutes a generalized eigenvalue problem [9].

III. RESULTS

A. Nonmagnetic convection

Unless noted otherwise, we put $R = \mathrm{Ra}/\mathrm{Ra}_c = 20$ and $\mathrm{Pr} = 1$. The number of possible 2D model combinations is large. We may set the velocity boundary conditions at the sidewalls to be either stress-free or nonslip, the radius of curvature of the top and bottom boundary to be either ∞ or $r_0/0.9$ (this radius may be varied continuously), the gravity and thermal basic state profiles to be either A or B, the form of v_r to be given either by Eq. (3a) or by Eq. (3b), and finally to include v_y or not. Already at this point we have $2^5 = 32$ possible models. In Fig. 2 we have chosen an economic path through model space that in our opinion well illustrates intermediate models between the classical annulus and the spherical shell.

The model settings in Fig. 2(a), see figure text, are comparable to those of the annulus model [8,9], and the results are similar. The $\langle N_p\rangle_t$ lines are closely spaced, i.e., the jets have about the same amplitude. In addition, $\langle N_p\rangle_t$ display a number of plateaux where each step is correlated with a depression of the zonal flow. However, compared to the 3D model in Fig. 2(f), both $\langle E_k\rangle_t$ and E_Z are being highly overestimated at low E. These quantities are better modeled with nonslip sidewalls, Fig. 2(b). The plateaux remain while the variation in jet amplitude increases. Introducing curvature of the top and bottom boundary has marked effects, Fig. 2(c). At low E, $\langle N_p\rangle_t$ increases, whereas $\langle E_k\rangle_t$ is being further reduced. At high E, the zonal flow strength E_Z increases. By changing the profiles of gravity and thermal basic state from A to B, we finally reduce $\langle E_k\rangle_t$ and E_Z to 3D levels at low E, Fig. 2(d). In terms of $\langle E_k\rangle_t$, E_Z, and $\langle N_p\rangle_t$, the effects of an improved v_r and the inclusion of v_y are small at low E, Fig. 2(e), see also below. However, these model refinements re-

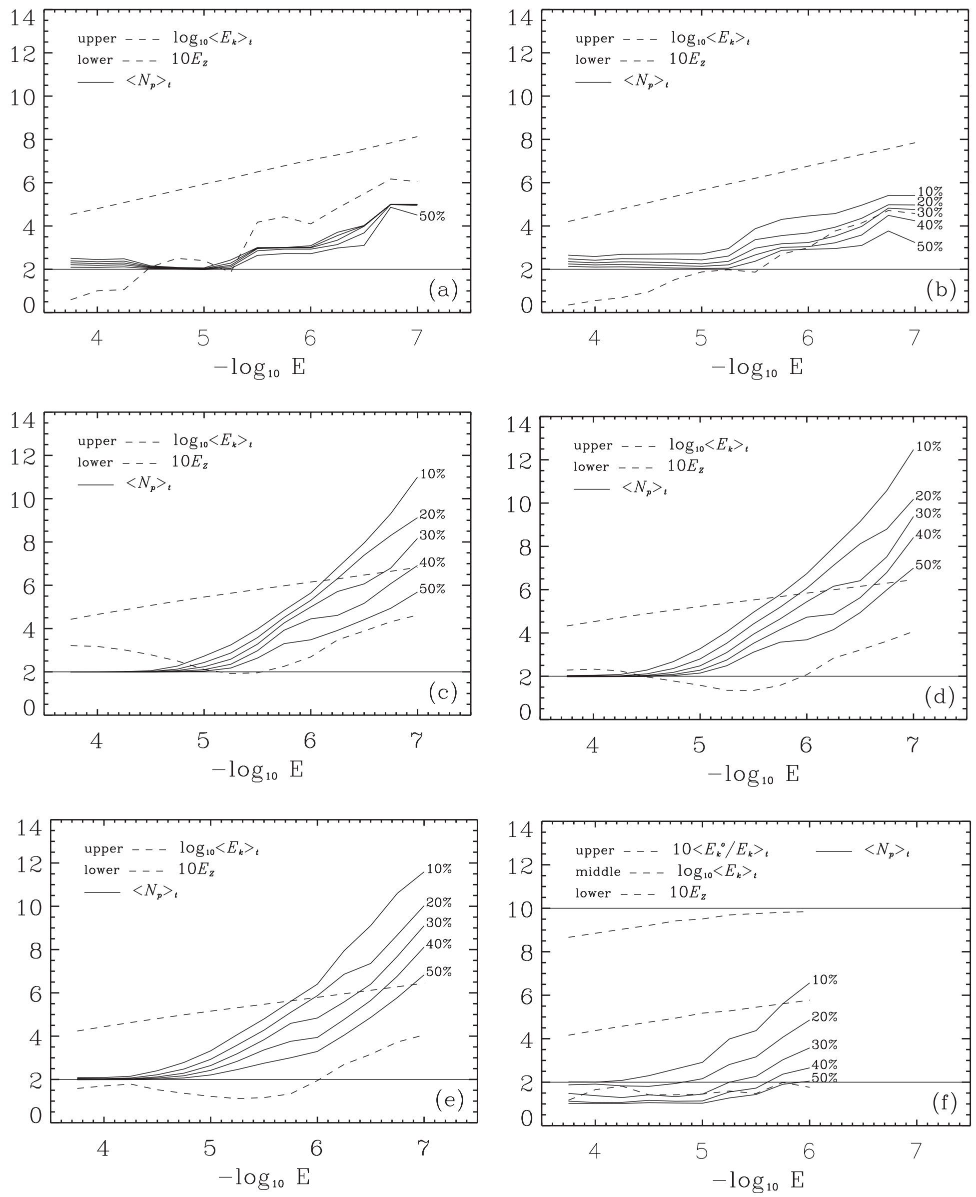

FIG. 2. Flow characteristics. Panels (a)–(e) display results of the 2D model. The upper dashed line is the kinetic energy $\log_{10}\langle E_k\rangle_t$. The zonal flow is defined as $u_Z=\langle u_x\rangle_x$. The lower dashed line depicts the strength of this flow component $10E_Z$, $E_Z=\langle E_k^Z/E_k\rangle_t$. From the radial zonal profile $\langle u_Z\rangle_z$ we determine the number of jets as follows: A jet is defined as a region whose endpoints are either at a profile endpoint or where $\langle u_Z\rangle_z$ is zero. The peak jet of $\langle u_Z\rangle_z$ is then found and the number of jets N_p, whose amplitude is more than p per cent of the peak jet, is determined. The result $\langle N_p\rangle_t$, where $p=10,20,\ldots,50$, is shown by solid lines. The horizontal through line depicts the classical two-jet solution. (a) 2D model, stress-free sidewalls, $r_0/r_T=0$, gravity and thermal basic state by profile A, v_r by Eq. (3a), and v_y neglected in Eq. (2a). (b) As in panel (a), but with nonslip sidewalls. (c) As in panel (b), but with $r_0/r_T=0.9$. (d) As in panel (c), but with gravity and thermal basic state by profile B. (e) As in panel (d), but with v_r by Eq. (3b), and v_y retained in Eq. (2a). (f) Results of the 3D model. In this model the zonal flow is defined as $u_Z=\langle u_\phi\rangle_\phi$ and the radial zonal profile as $\langle u_Z\rangle_z$. The two lowermost dashed lines and the five solid lines are calculated outside the TC as in the 2D model. The upper dashed line is the energy outside the TC compared to the total energy, $10\langle E_k^0/E_k\rangle_t$. The upper through line depicts the 100% level of this quantity.

duce E_Z further towards 3D levels at high E. The general agreement of the latter 2D model with the 3D model is good. The number of jets $\langle N_p\rangle_t$ is closest to the 3D result when p is small. However, the slope of $E_Z(E)$ at $E=1\times10^{-6}$ is being overestimated. We attribute this to the missing heat transport along the rotation axis of the 2D model, suggesting that R_{2D} should be smaller than R_{3D}, see below. For all 2D models the multijet solutions emerge roughly at the same $E=5\times10^{-6}$ as in the 3D model. In the following, the 2D model of Fig. 2(e) is referred to as model I and the 3D model of Fig. 2(f) is denoted model II.

At $E=1\times10^{-7}$, model I produces a multijet azimuthal flow with moderate strength, Fig. 3(a). The jets are strongest close to the TC. In addition, the prograde jets tend to be wider than the retrograde jets. A remarkable phenomenon is displayed in Fig. 3(b) where three regions with different jet

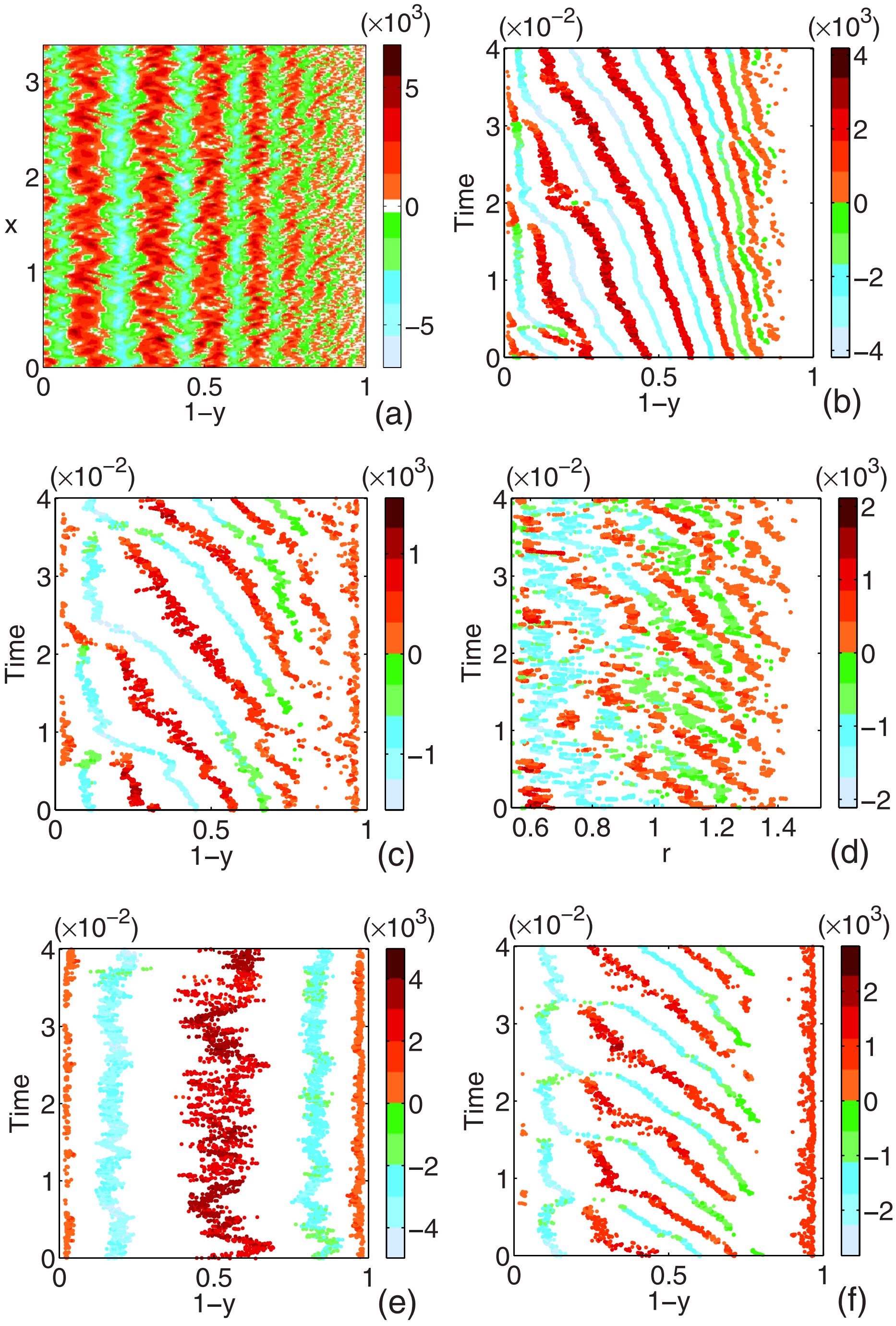

FIG. 3. (Color online) Zonal flow and its extrema. (a) — (c) show the solutions of model I. (a) Snapshot of u_x displaying ~10 jets, $E=1\times10^{-7}$, and two-fold x symmetry (2-FXS). E_Z=41%. (b) Time-dependent extrema of the radial zonal profile stronger than 10% of the peak jet. Same parameters as in panel (a). (c) As in panel (b), but for $E=1\times10^{-6}$ and 1-FXS. E_Z=19%. Panel (d) displays the solution of model II at $E=1\times10^{-6}$ and eightfold azimuthal symmetry (8-FAS). E_Z=18%. In panel (e) is shown zonal flow extrema produced by the 2D model in Fig. 2(b) at $E=1\times10^{-6}$ and 1-FXS. E_Z=30%. (f) As in panel (e), except that the model is that of Fig. 2(c). E_Z=27%.

dynamics may be observed. The center region II, $y\in[0.3,0.7]$, contains ~5 jets that are drifting towards the TC at a rate ~10 at mid-depth. Note that the drifting motion applies to the extrema of the radial zonal profile which may be approximately described by the form $\langle u_Z\rangle_z=f(s)\cos[k(s)s+\omega t]$. Here f is a decreasing function of the distance s to the z axis. The drift speed ω/k is higher closer to the TC where the jets are wider. In the outer region III, $y<0.3$, the azimuthal flow is weak and has no clear jet structure. In the inner region I, $y>0.7$, the jets are changing their width, being created or destroyed, and sometimes change their drift rate abruptly. From time to time the jet next to the TC may become prograde for a short while instead of the normal retrograde motion. In order to verify this new phenomenon by the numerically more expensive model II we have carried out a comparison at $E=1\times10^{-6}$, see Figs. 3(c), 3(d). Even at this relatively high Ekman number where the number of jets is small the three-region structure is evident in both models, see also below for further 3D confirmations. In Fig. 3(c) we note that the zonal flow suppression in region III, especially of the prograde jet close to $y=0$, is less pronounced than in model II. The same applies to the model of Fig. 2(d). However, the use of Eq. (3b) and the inclusion of v_y in the Coriolis term result in efficient suppression of the zonal flow in region III provided that the Ekman number is sufficiently small, $E<2\times10^{-7}$, see Fig. 3(b). This is reasonable since $\theta\sim1$ in this region. In general, the third Coriolis subterm is neglected in quasigeostrophic models. The jet drift phenomenon is not observed in the classical annulus irrespective of the velocity boundary conditions at the top and bottom boundary [8,9]. In these models localized fluctuations of the azimuthal flow may appear in terms of thermal Rossby waves excited by convective bursts. In the model of Fig. 2(a), which is close to the annulus model of Refs. [8,9], the jet drift is also absent. However, by imposing nonslip sidewalls which results in the model of Fig. 2(b), we introduce marked fluctuations of the zonal flow extrema, see Fig. 3(e). In this model, which has the same weakly varying $H(y)$, but a weaker zonal flow than in the model of Fig. 2(a), one of the five calculated solutions for $E\in[1\times10^{-7},1\times10^{-6}]$ has drifting jets. A strongly varying $H(y)$, however, results consistently in jet drift, see Fig. 3(f). This model property, in addition to nonslip top and bottom boundaries that enable multijet solutions, seems to be crucial to the occurrence of jet drift. In the 2D model the radius of curvature of the top and bottom boundary may be varied continuously. This free parameter may in principle be used to determined the critical radius of curvature for onset of jet drift. By comparing the drift speeds in Figs. 3(c), 3(d) we notice that the drift rate in model II is approximately twice that of model I. The importance of a strongly varying $H(y)$ to the jet drift suggests that this difference in drift speed is to due to the missing azimuthal curvature of model I.

As function of driving strength R the zonal flow dynamics in model I may be seen in Figs. 4(a)–4(g). At $(R,E)=(2.5,1\times10^{-7})$ the width of region III is 0.7, and only ~4 jets are observed. By increasing $R=5$, 10, region III narrows and the number of jets increases. The zonal flow remains weak, $E_Z\leq6\%$. The case $R=20$ is shown in Figs. 3(a), 3(b). By $R=40$, region III has vanished, but the width of region I is as for $R=20$. The number of jets has begun to decrease, see also Fig. 5(c), whereas the drift rate in region II has increased. At $R=80$, the width of region I has grown to 0.8, and faster jet drift in the bulk of this region is observed. At $R=160$, region II has vanished. Only a few jets are left, but they are drifting faster in the bulk of Region I. The center jets have begun to weaken. This tendency has become more pronounced at $R=320$. Eventually, at still higher R, the center jets will vanish leaving only two strong steady jets with fluctuating extrema. At $E=3.16\times10^{-7}$ and 1×10^{-6}, this happens at a lower R, Figs. 4(h),4(i). As expected, this solution, which has reduced Ekman layer effects, resembles the two-jet solutions obtained with stress-free boundaries in models of e.g., Jupiter's atmosphere [2,3]. An example of the R dependence of the solutions in model II is given by Figs. 3(d) and 4(j),4(k). We note that the above scenario for model I at $E=1\times10^{-7}$ is confirmed although it happens faster in R due to the lower number of jets. As for model I, the jet depletion in the center region at high R may be counteracted by decreasing the Ekman number, Fig. 4(l).

For $E\in[1\times10^{-7},1\times10^{-6}]$, we find $E_Z\leq6\%$ when $R\leq10$, see Fig. 5. At $R=10$, the zonal flow strength $E_Z(R)$ displays a kink and begins to grow steeply, its slope increasing with decreasing Ekman number. Eventually, $E_Z(R)$ saturates at high R where also zonal relaxation oscillations may appear [9]. Thus Fig. 5 suggests that the slope of $E_Z(E)$ at $\mathrm{E}=1\times10^{-6}$ is smaller for $R<20$ than at $R=20$. As proposed above, this provides an explanation of the relatively large slope of $E_Z(E)$ at $\mathrm{E}=1\times10^{-6}$ in model I as compared to model II.

As suggested by Fig. 2(e), the jet number scales excellently with the Ekman number when $E<5\times10^{-6}$. Setting $\langle N_p\rangle_t\propto E^{\lambda_p}$, we find $(\lambda_{10},\lambda_{20},\lambda_{30},\lambda_{40},\lambda_{50})=-(0.27,0.25,0.25,0.25,0.26)$. These scalings may be related to Rhines length scale $L_R\propto(U/\beta)^{1/2}\propto(EU)^{1/2}$ of a flow component having velocity U [15]. In our model I, β (>0) is minus the coefficient in front of the first Coriolis subterm of Eq. (2a). For $E<5\times10^{-6}$ the kinetic energy $\langle E_k\rangle_t\propto E^{-0.65}$. The corresponding $L_R\propto E^{0.34}$, which is close to the length scale on which convection operates [9]. This result is consistent with the fact that the zonal flow is relatively weak for $E>1\times10^{-7}$. For $E<5\times10^{-6}$ the zonal energy $\langle E_k^Z\rangle_t\propto E^{-1.02}$, and the related $L_R^Z\propto E^{0.25}$. This Rhines length scale, which determines the endpoint of an inverse energy cascade maintained by azimuthal mean Reynolds stresses, fits the scaling of $\langle N_p\rangle_t$. At $E=1\times10^{-7}$, the zonal flow length scale at the TC is 3.8 times larger than the convective length scale, as $l_c=64$ at onset of convection. Interestingly, an $L_R^Z\propto E^{1/4}$ scaling may also be obtained in a weakly nonlinear 1.5D model, and explained by a balance between Reynolds stress, Ekman and bulk dissipation in the zonal flow equation [16]. From the Rhines length scale argument we expect that (i) due to an increased β parameter and a reduced zonal flow strength, the (many) jets will narrow as function of distance from the TC, see Fig. 3(a), and (ii) caused by an increased zonal flow strength, the number of jets as function of R will eventually begin to decrease and reach a low number, see Fig. 5.

B. Convective kinematic dynamos

We conclude this paper by making some important applications of the above results to planetary dynamos. The first systematic study of convection-driven geodynamo models displaying a reversing dipole at the core-mantle boundary appeared in Ref. [17]. They show that a necessary condition for reversals is that the magnetic energy is smaller than the kinetic energy. In addition, a further increase of the driving strength may be necessary. In nonreversing dipolar dynamos driven by the thermal modus of the present paper, the Lorentz force $\mathbf{F}_m=(1/\mathrm{Pm})(\boldsymbol{\nabla}\times\mathbf{B})\times\mathbf{B}$ tends to damp (enhance) the relative strength of the zonal flow outside (inside) the TC

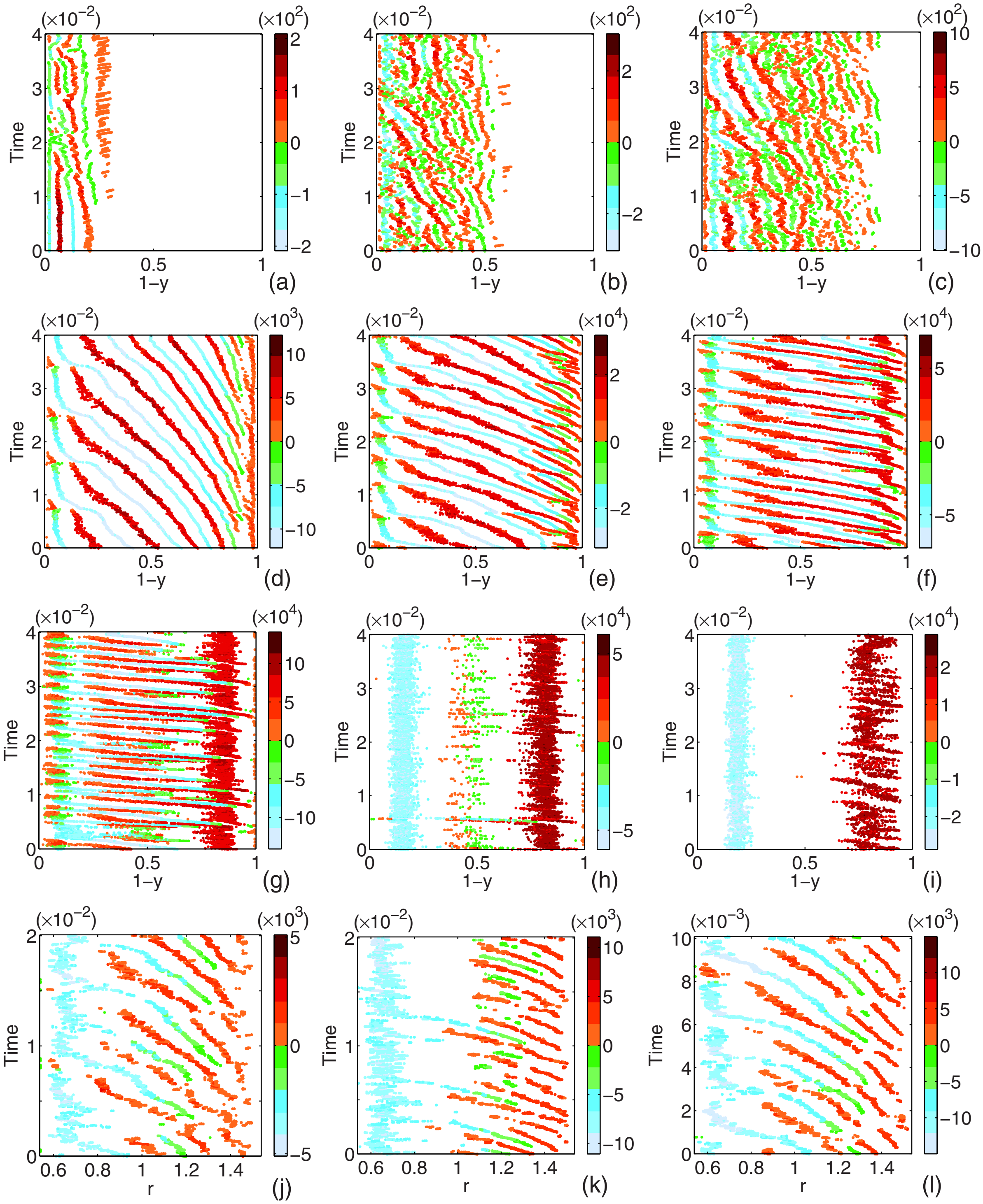

FIG. 4. (Color online) Zonal flow extrema as function of the forcing level R and Ekman number E. Panels (a)–(g) show solutions of model I at $E=1\times10^{-7}$ and 2-FXS. The driving is $R=2.5$, 5, 10, 40, 80, 160, and 320; and the zonal flow strength $E_Z=6$, 4, 5, 57, 61, 65, and 68 %, respectively. Note that the case $R=20$ is shown in Fig. 3(b). As in panel (g), the solutions in panels (h), (i) are from model I at $R=320$, but with $E=3.16\times10^{-7}$, 2-FXS, $E_Z=58\%$; and $E=1\times10^{-6}$, 1-FXS, $E_Z=53\%$, respectively. Finally, in the last row, solutions of model II are depicted. The three solutions have $(R,E,E_Z,FS)=(40,1\times10^{-6},29\%,3\text{-FAS})$, $(80,1\times10^{-6},41\%,3\text{-FAS})$, and $(80,5.62\times10^{-7},45\%,4\text{-FAS})$, respectively.

[18]. Here **B** is the magnetic field and $\mathrm{Pm}=\nu/\eta$ is the magnetic Prandtl number, η being the magnetic diffusivity. However, for reversing dynamos at moderate E, the flow changing effects of $\mathbf{F}_m$ is reduced both inside and outside the TC [18]. Due to computational costs we focus below on kinematic dynamos, hence neglecting $\mathbf{F}_m$.

We impose electrical insulators outside the spherical shell and solve the magnetic induction equation

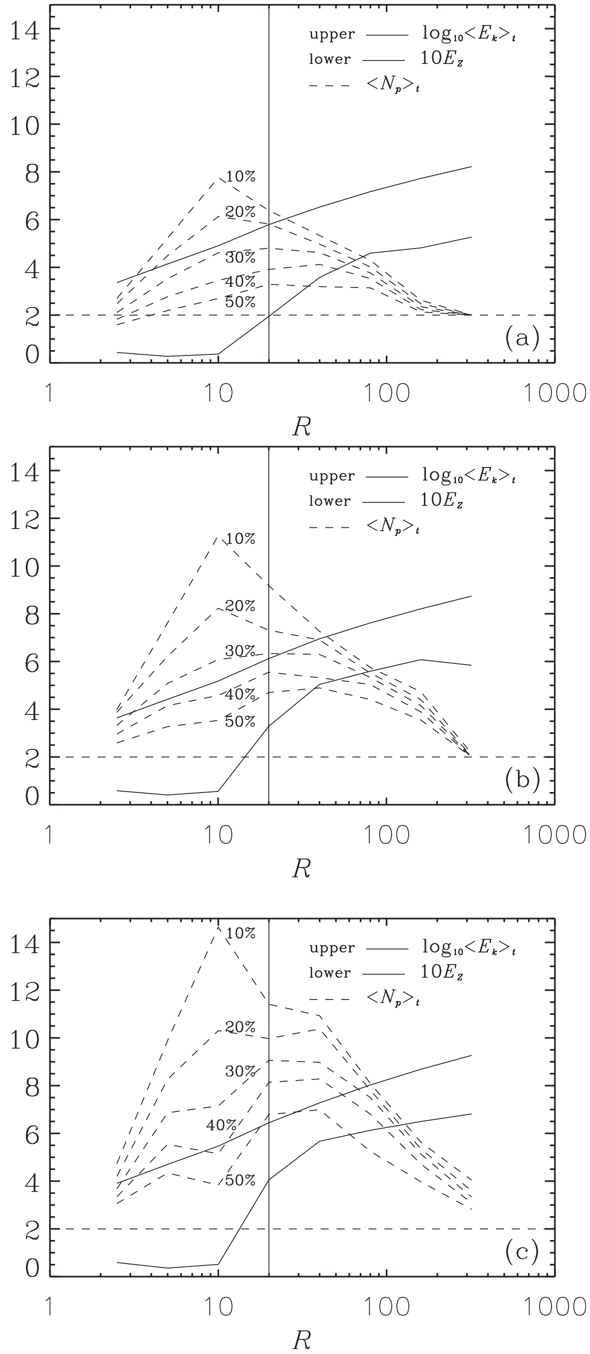

FIG. 5. Flow characteristics of model I as function of forcing level R and Ekman number E. The line definitions are identical to those of Figs. 2(a)–2(e) except for a linestyle swap in order to highlight the kinetic energies. The three panels have $E=1\times10^{-6}$, 3.16×10^{-7}, and 1×10^{-7}, respectively. The vertical auxiliary line indicates $R=20$.

$$\frac{\partial\mathbf{B}}{\partial t}=\nabla\times(\mathbf{u}\times\mathbf{B})+\frac{1}{\mathrm{Pm}}\nabla^2\mathbf{B}. \tag{7}$$

The velocity $\mathbf{u}$ is taken as the above 3D time-dependent convective flows and we search for quasiexponentially growing solutions with Pm close to Pm_c for onset of dynamo action. We have solved at $(E,\mathrm{Pm})=(1\times10^{-4},0.8)$, $(1\times10^{-5},0.45)$, and $(3.16\times10^{-6},0.3)$, where the zonal flow strength outside the TC is $E_Z=\langle E_k^{Z,0}/E_k^0\rangle_t=17$, 15, and 15 %, respectively, see Fig. 2(f). The relatively large-scale convection at high E implies good mixing and absence of persistent large-scale coherent structures in B_r at $r=r_0$. However, at the lowermost E, two interleaved magnetic spirals have emerged, Fig. 6(b). This solution is antisymmetric in the equatorial plane and has a slow prograde drift. The sign of the spiral is due to the advection of magnetic field lines by the strong retrograde jet at the TC; see Fig. 6(a), but more pronounced at the higher $E=3.16\times10^{-6}$. The toroidal magnetic field of the kinematic dynamos becomes increasingly dominant at lower E, its energy being $\langle E_m^{\mathrm{tor}}/E_m\rangle_t=61$, 67, and 74 % in the three cases. The constant $E_Z\sim15\%$ suggests that the enhanced toroidal field is due to the increased shear caused by the multijets emerging at $E\sim5\times10^{-6}$.

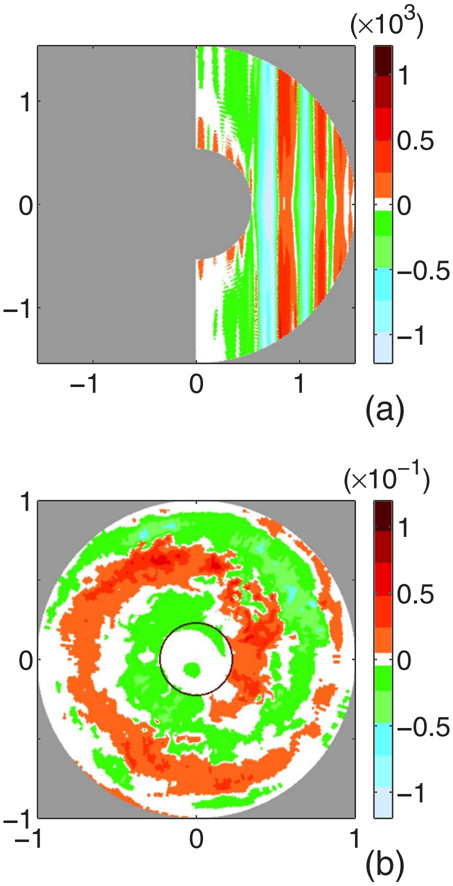

FIG. 6. (Color online) Solutions of model II. (a) Snapshot of the zonal flow having ~6 jets outside the TC. $(E,FS)=(1.78\times10^{-6},8\text{-FAS})$. (b) Kinematic dynamo. The radial component of the magnetic field B_r at $r=r_0$ is seen from the northern hemisphere. The colatitude θ is a linear function of radius, which makes the TC (black line; brown line online) appear relatively smaller than in panel (a). $(E,\mathrm{Pm},FS)=(3.16\times10^{-6},0.3,1\text{-FAS})$.

The possibility of signatures in the magnetic field created by the drifting jets is currently being investigated. Using the filtering method in Ref. [18], it may be shown that the main dynamo region of the kinematic dynamo at $(R,E,\mathrm{Pm},FS)=(40,1\times10^{-6},0.064,9\text{-FAS})$, is located in the cylindrical shell $s \in r_i + [0.2, 0.3]$, see also Fig. 4(j). The magnetic Prandtl number is slightly above critical. The α-effect in the dynamo region is created by the Busse columns. The drifting jets imply a time-dependent ω effect in the dynamo region when the jets are moving through it. This is likely to result in a time-dependent efficiency of the dynamo hence creating variations in the field intensity and making it possible to detect the jet drift outside the shell. For the above kinematic dynamo this effect is observed as kinks of the otherwise quasiexponentially growing magnetic energy.

In summary, we have in this paper investigated the zonal flow in a rotating convecting spherical shell with nonslip boundaries by means of a 3D model and a 2D generalized annulus model for the region outside the TC. The latter model has been evaluated in configurations spanning from a setup approximating the classical annulus to a close approximation of the 3D shell. This allows a separation of effects in terms of individual model features. A type of zonal flow with multiple inwardly drifting jets has been found and confirmed using fully independent models. This type of flow will affect geodynamo models at high rotation rate and thermal driving.

ACKNOWLEDGMENTS

The computational work was performed on the Linux clusters (Opteron 2.2 GHz, Xeon 3.0 GHz) at the GWDG calculation center in Göttingen, funded by Niedersachsen and the Max-Planck-Society. In addition, usage was made of the central Linux cluster (Opteron 2.4 GHz) at ETH Zürich, which in part is funded by the GFD group at Institut für Geophysik in Zürich. Finally, computations were performed on the Cray XT3 (Opteron 2.6 GHz) at the CSCS Swiss National Supercomputing Center in Lugano. This usage is supported by a Swiss Alps supercomputing grant.

[1] F. H. Busse, Icarus **20**, 255 (1976).
[2] U. R. Christensen, Geophys. Res. Lett. **28**, 2553 (2001).
[3] M. H. Heimpel, J. M. Aurnou, and J. Wicht, Nature (London) **438**, 193 (2005).
[4] J. M. Aurnou and M. H. Heimpel, Icarus **169**, 492 (2004).
[5] J. B. Manneville and P. Olson, Icarus **122**, 242 (1996).
[6] J. Aubert, N. Gillet, and P. Cardin, Geochem., Geophys., Geosyst. **4**, 1052 (2003).
[7] N. Gillet and C. A. Jones, J. Fluid Mech. **554**, 343 (2006).
[8] C. A. Jones, J. Rotvig, and A. Abdulrahman, Geophys. Res. Lett. **30**, 1731 (2003).
[9] J. Rotvig and C. A. Jones, J. Fluid Mech. **567**, 117 (2006).
[10] S. Stanley, J. Bloxham, W. E. Hutchison, and M. T. Zuber, Earth Planet. Sci. Lett. **234**, 27 (2005).
[11] U. R. Christensen *et al.*, Phys. Earth Planet. Inter. **128**, 25 (2001).
[12] J. Rotvig and C. A. Jones, Phys. Rev. E **66**, 056308 (2002).
[13] H. P. Greenspan, *The Theory of Rotating Fluids* (Cambridge University Press, Cambridge, 1968).
[14] J. Tao and F. H. Busse, J. Fluid Mech. **552**, 73 (2006).
[15] P. B. Rhines, J. Fluid Mech. **69**, 417 (1975).
[16] V. Morin and E. Dormy, Phys. Fluids **18**, 068104 (2006).
[17] C. Kutzner and U. R. Christensen, Phys. Earth Planet. Inter. **131**, 29 (2002).
[18] J. Rotvig (unpublished).